Using orthographic projection with geographic information system (GIS) data to constrain the kinematics the Central Range Fault zone, Trinidad

Scott Giorgis [a,*], John Weber [b], Jenna Hojnowski [a], William Pierce [a], Anthony Rodriguez [b]

[a] Department of Geological Sciences, SUNY Geneseo, 1 College Circle, Geneseo, NY 14454, USA
[b] Geology Department, Grand Valley State University, One Campus Drive, Allendale, MI 49401-9403, USA

ARTICLE INFO

ABSTRACT

Fold geometry versus axis orientation can be used to constrain the kinematics of transpressional plate boundaries. This approach is typically based on bedding orientation data collected in the field, however, in some regions outcrop quality is insufficient to provide enough measurements. We extract orientation data from a georeferenced geologic map and a digital elevation model and to constrain the kinematics of a poorly exposed, active transpressional boundary: the Central Range Fault zone in Trinidad. Strike-and-dip orientations are calculated based on contact positions extracted from the digital geologic and topographic datasets. The uncertainties in the both horizontal position and elevation of the contact are propagated into the final kinematic analysis. Analysis of folds adjacent to the Central Range Fault suggests the angle of oblique convergence in transpression (α) varies from 20° to 85°. The majority of folds, however, are consistent with a large component of contraction (i.e. $\alpha > 50°$). The analysis also suggests folding in the Central Range records a minimum of 3–9 km of contraction, 3 km of strike-slip motion, and 4–9 km of total plate motion. The range of values reflects uncertainties in the position of the folded contacts. We interpret the overall kinematics of deformation, amount of shortening, and homogeneity of the finite strain field to indicate that active deformation on the Central Range Fault zone has not yet accumulated enough strain to overprint the effects of earlier (pre-strike-slip; pre-Middle Miocene) fold-and-thrust style tectonics.

© 2011 Elsevier Ltd. All rights reserved.

1. Introduction

High strain strike-slip fault systems with a component of oblique convergence, such as the San Andreas Fault system, typically partition deformation between the main fault the adjacent borderlands (e.g. Zoback et al., 1987; Jamison, 1991; Teyssier and Tikoff, 1998). In general, most of the strike-slip component of deformation is accommodated by the central fault, and the borderlands absorb most of the contraction (e.g. Teyssier and Tikoff, 1998; Titus et al., 2007). The kinematics of the borderlands can thus reflect a combination of convergence and strike-slip motion — i.e. transpression. The relative contribution of strike-slip motion vs. convergence has previously been investigated by examining folded strata in the borderlands (e.g. Jamison, 1991; Tikoff and Peterson, 1998; Titus et al., 2007). These studies provided important information about the kinematics and strike-slip partitioning across well-exposed, active transpressional plate boundaries.

Previous work on the San Andreas Fault system focused on well-exposed, arid segments and used bedding orientation data to characterize fold geometry and orientation in the borderlands (e.g., Jamison, 1991). In deeply weathered and heavily vegetated regions, such as in the Central Range in Trinidad, poor exposure limits how much bedding data can be collected. However, if detailed geological mapping exists, such as in Trinidad where the surface mapping was based on extensive micropaleontological augering (Kugler, 1960), it is possible to use the intrinsic relationship between contacts and topography to determine fold geometry. The utility of this approach is limited only by the accuracy of the geologic map and of the elevation data set.

We present a kinematic analysis of the Central Range Fault zone — i.e. the Central Range Fault itself and the adjacent borderlands — in Trinidad that used orthographic projection to analyze digital geologic map and elevation datasets using ArcGIS and MatLab. The approach developed and presented here includes a numerical method to propagate uncertainty in contact position into the final results. Our study of the Central Range Fault zone illustrates the potential and limitations of using GIS-based orthographic projection as a tool for kinematic analysis.

* Corresponding author. Tel.: +1 585 245 5293.
E-mail address: giorgis@geneseo.edu (S. Giorgis).

2. Geologic setting

Trinidad is located along the South American-Caribbean plate boundary. Obliquely convergent motion of the Caribbean Plate relative to South America throughout much of the Cenozoic resulted in an orogen active first in western South America and then progressively further east (e.g., Speed, 1985; Pindell et al., 1998). Fig. 1 shows the generalized geology of Trinidad. The Northern Range, contains largely metasedimentary rocks with Mesozoic protolith ages and Cenozoic metamorphic ages, and comprises the exhumed hinterland segment of this orogen (Weber et al., 2001a). The Late Cretaceous sediments currently exposed in central Trinidad were deposited in a passive margin setting, while the Paleogene-Early Neogene section was deposited in a distal foreland basin in front of the advancing orogen. Late Pliocence to Pleistocene sediments and sedimentary rocks in Trinidad are largely deltaic deposits of the paleo-Orinoco system. On the north flank of the Central Range, the Late Neogene-Pleistocene section was deposited unconformably after intense folding and thrusting deformed the pre-Middle Miocene strata. In south Trinidad, folding continued into the Pleistocene.

Sometime between ~12 Ma and the present, Caribbean-South American plate tectonics changed from oblique convergence to transform motion, with local transpression and transtension; active transtension occurs in the Gulf of Paria pull-apart basin, and active transpression in expected in central Trinidad (Pindell et al., 1998; Weber et al., 2001b). Geodetic (GPS) analysis showed that the Caribbean plate is presently moving 20 mm/yr due east relative to a fixed South American plate (Perez et al., 2001; Weber et al., 2001b). West of Trinidad, in Venezuela, most of this motion is accommodated on the El Pilar Fault (Perez et al., 2001). In Trinidad, the locus of plate motion steps south off of the El Pilar Fault onto the Central Range Fault (Saleh et al., 2004; Weber et al., 2011). In addition, the geodetic analyses showed that 12 ± 3 mm/yr of the total 20 mm/yr relative plate motion is accommodated on the Central Range Fault (Weber et al., 2011). The Central Range Fault strikes 070°, which is ~20° oblique to the Caribbean-South American relative plate motion vector, and the modern elastic strain field centered on the fault is approximately 30 km wide (Weber et al., 2011). Motion at 12 mm/yr in this orientation resolves into 4 mm/yr of zone-normal convergence. Overall, the Central Range is characterized geologically as an anticlinal flower structure that exposes Late Cretaceous sedimentary rocks in its core and Oligocene to Miocene strata on its flanks (Fig. 1; de Verteuil et al., 2006). These units are generally unmetamorphosed, and reset apatite fission track data demonstrate these rocks reached temperatures greater 130 °C and experienced exhumation primarily in the Miocene (Sanguinito et al., 2010). The unconformably overlying Late Pliocene to Pleistocene section is tilted northward off the north flank of the Central Range and also forms most of the surficial geology and fill of the oil-rich Southern Basin (Fig. 1).

Folding and faulting in the Central Range clearly indicate this region has experienced Middle Miocene contraction, e.g. the geologic reconstructions of Pindell et al. (1998). The presence and spatial pattern of the Early to Middle Miocence shallow-water Tamana Limestone in the Central Range indicate limited emergence of the fold-thrust belt at paleo-topographic (and structural?) culminations (Erlich et al., 1993). Geodetic data suggest that contraction could be active today (e.g., Weber et al., 2011). The clear geomorphic expression of the Central Range Fault, observations from paleoseismic trenching, and offsets imaged in offshore 3D seismic data all suggest that transpressional activity was also likely active earlier in the Holocene (Soto et al., 2007; Prentice et al., 2010; Weber et al., 2011). It is uncertain, however, how much of the folding, faulting, and topography in the Central Range is due to pre-Middle Miocene convergence vs. Holocene transpression (Weber et al., 2011). Given this complexity, it is also likely that the Central Range may record more than one generation of deformation and/or reactivation.

In this study we used the macroscopic, second order folds on the flanks of the anticlinal flower structure in the Central Range to characterize the kinematics of deformation and estimate finite strain. The Central Range folds plunge gently, and are upright, tight-open, NE-trending, and outcrop in bands that are 1−2 km in length and several hundred meters wide. Outcrop is scarce in the Central Range, however good quarry exposures in the reef carbonates of the Tamana Formation suggest that open, sinusoidal, constant-thickness, flexure-slip folds predominate there. Our analysis, which focused on second order folds, does not take into account shortening due to thrust faults or larger order folding, therefore our results represent minimum strain estimates. Lastly, we calculate finite strain, which provides only a sum of Miocene and modern shortening.

3. Kinematic model of folding in transpression

3.1. Data collection

Our initial data set consisted of a georeferenced geologic map and a digital elevation model (DEM) of Trinidad (de Verteuil et al., 2006). Contact location data were collected in the Universal Transverse Mercator (UTM) system (Zone 20 for Trinidad). Our coordinate system is set with the *x*-axis oriented east−west, parallel to UTM easting, the *y*-axis north−south, parallel to UTM northing, and the *z*-axis up-down. Using ArcGIS, we generated a table of *x*, *y*, and *z* coordinate points that followed each folded contact (Fig. 2).

3.2. Contact orientation

The orientation of a folded contact can be determined at any locality along its trace using three adjacent points via orthographic projection. Assuming that the contact is locally planar, the trend and plunge of the pole to that plane can be calculated by converting those three points into two vectors (**A** and **B**), and then taking the cross product of those vectors (e.g. Ragan, 2009). Vector **A** was created by connecting the point with the highest elevation to the point with the lowest elevation. Similarly, vector **B** was created by connecting the intermediate elevation point with the lowest elevation point. The orientation of vectors **A** and **B** can be described using the direction cosines [*l m n*]. A vector with a trend *T* and a plunge *P* has direction cosines

$$[l, m, n] = (\cos P \cdot \cos T \quad \cos P \cdot \sin T \quad \sin P) \qquad (1)$$

(e.g. Charlesworth et al., 1976). The cross product of these two vectors yielded the direction cosines of the pole to the plane containing these three points. These direction cosines were then converted back into trend and plunge. This process was then repeated along the contact using each possible combination of three consecutive points.

3.3. Fold axis

An analytical solution to the calculation of a fold axis from a population of poles to bedding is given by Charlesworth et al. (1976). Briefly, a population of *p* poles are converted to direction cosines using eq. (1) and then used to calculate the matrix
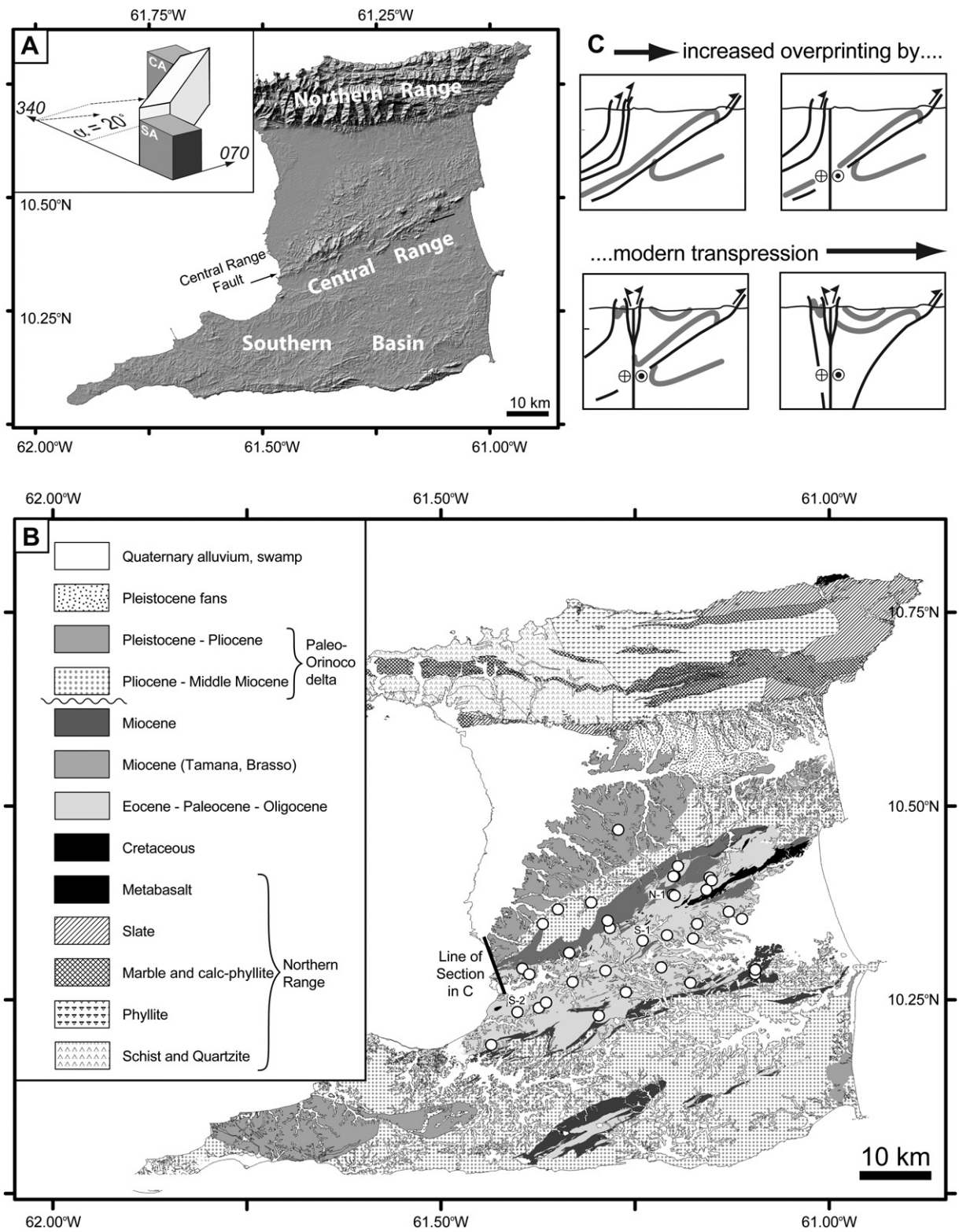
Fig. 1. (A) Shaded relief map of Trinidad (de Verteuil et al., 2006). Inset: Block diagram illustrating the transpressional kinematics that characterize modern deformation. (B) Simplified geological map from de Verteuil et al. (2006). The numerous faults mapped in Central Range and elsewhere were omitted to highlight the island's general geology. Dots represent locations of folds analyzed in this study. Only those shown explicitly in Figs. 2 and 8 are labeled. See Table 1 for a full set of locations. (C) NW (left) to SE (right) oriented cross sections illustrating a range of possible interpretations of the subsurface geometry of the Central Range adapted from Kugler (1960) and Babb and Mann (2000). See (C) for line of section.
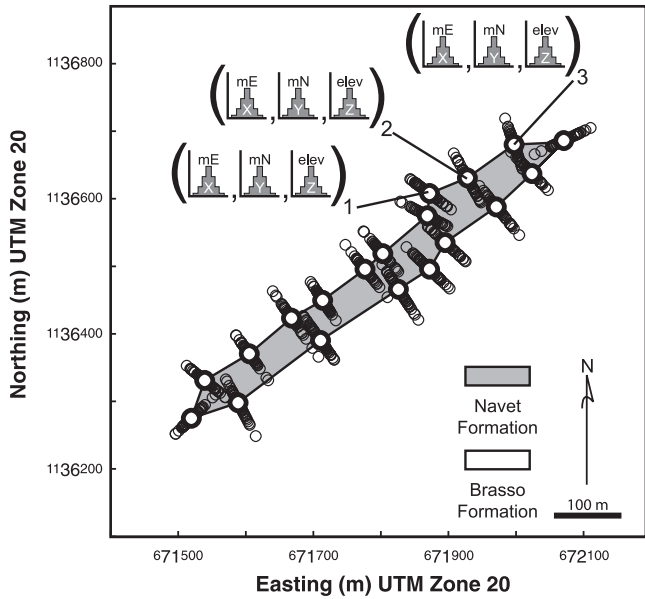
Fig. 2. Simplified geologic map of a fold S-1. See Fig. 1 and Table 1 for location. The bold, open black circle marks the position of the coordinates extracted from the ArcGIS database and the DEM. Scatter of small, open circles on either side of the mean illustrate the geographic extent of the *x* and *y* uncertainties. The histograms schematically show the normal Gaussian distribution of *x*, *y*, and *z* positions considered in the orientation calculations. Geologic map modified from de Verteuil et al. (2006).

$$T = \begin{pmatrix} \sum_{i=1}^{p} l_i^2 & \sum_{i=1}^{p} l_i m_i & \sum_{i=1}^{p} l_i n_i \\ \sum_{i=1}^{p} l_i m_i & \sum_{i=1}^{p} m_i^2 & \sum_{i=1}^{p} m_i n_i \\ \sum_{i=1}^{p} l_i n_i & \sum_{i=1}^{p} m_i n_i & \sum_{i=1}^{p} n_i^2 \end{pmatrix}. \qquad (2)$$

Matrix T has three eigenvectors and eigenvalues. The eigenvector paired with the minimum eigenvalue is the orientation of the fold axis (Charlesworth et al., 1976).

3.4. Strain recorded by folds

For simplicity, we assume that contraction in the Central Range borderlands produced only constant thickness, constant bed length, symmetric sinusoidal folds. The additional effects of asymmetric structures and faulting are considered in the discussion below. For sinusoidal folds, there is a simple and direct relationship between either the maximum limb dip or the average bedding dip and the total amount of shortening recorded by that fold (Fig. 3;

Jamison, 1991). We use the phrase "average bedding dip" to refer to the mean of a population of dip measurements taken from a single fold (Fig. 3). Average bedding dip is used in our numerical model rather than maximum limb dip because maximum limb dip is sensitive to a single orientation estimate while average bedding dip relies on the entire orientation population.

3.5. Angle of oblique convergence

The angle of oblique convergence (α) is defined as the acute angle between the plate boundary and the plate motion vector and can vary from $0°$ (pure strike-slip) to $90°$ (pure convergence) (Sanderson and Marchini, 1984). Jamison (1991) developed a relationship between fold axis orientation, percent shortening, and the angle of oblique convergence (Fig. 4), with the coordinate system aligned parallel to the boundaries of the transpressional system, which are assumed to be parallel to the master strike-slip fault (Fig. 1). In transpression, a fold axis will initiate perpendicular to the minimum infinitesimal stretching direction (Graham, 1978; Odonne and Vialon, 1983; Tikoff and Peterson, 1998). The orientation of the minimum infinitesimal stretch direction is a direct function of the angle of oblique convergence (e.g. Teyssier et al., 1995). Therefore the angle (θ) between the boundary of the transpressional zone and a fold axis is directly related to the angle of oblique convergence.

After initial formation of a fold, the fold axis is a finite stain marker that rotates at a rate determined by the angle of oblique convergence (Jamison, 1991; Titus et al., 2007). In a purely contractional setting ($\alpha = 90°$), a fold axis initiates parallel to the shear zone boundary and remains in that orientation (Fig. 4). In purely wrench settings folds initiate at $45°$ to the shear zone boundary and progressively rotate into parallelism with the boundary. Intermediate angles of oblique convergence (i.e. $0° < \alpha < 90°$), the rate of rotation of the fold axis is higher for strike-slip dominated systems. However, with enough deformation, all fold axes will end up parallel to the shear zone boundary (Fig. 4).

The relationships displayed in Fig. 4a assume that fold axes rotate as active markers. In models taking this approach, the fold axis remains parallel to the maximum stretching direction throughout deformation (e.g., Titus et al., 2007). Alternatively, fold axes could be treated as material lines, which rotate faster than the axis of the finite strain ellipse (Lister and Williams, 1983). Following Titus et al. (2007), we favor the active rotation model because: (1) it is supported by both theoretical and physical experiments (Treagus and Treagus, 1981; Tikoff and Peterson, 1998); and (2) it provides a minimum estimate of the strain recorded by folding in the borderlands (see Titus et al. (2007) for a complete discussion). The effects of passive model rotation are considered in the discussion below.
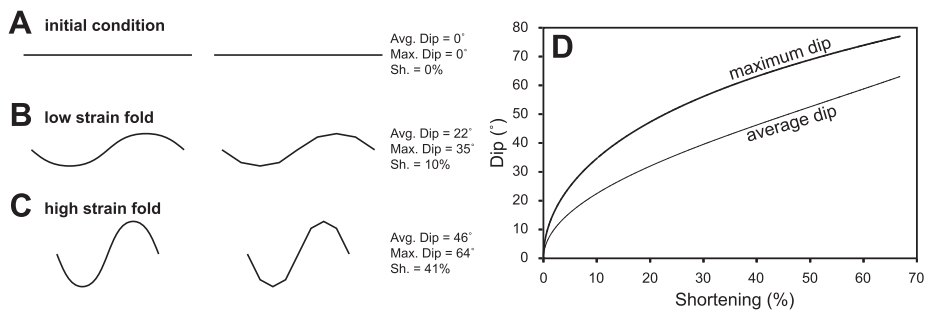
Fig. 3. Relationship between dip and percent shortening for sinusoidal folds. An initially flat layer (A) has a zero degree dip and zero shortening. Folding this layer into a low amplitude sinusoidal fold increases the dip and the shortening (B). An average bedding dip, maximum bedding dip, and percent shortening for the fold are calculated by breaking the fold into eight discrete straight line segments. Application of the same procedure to a high amplitude fold yields higher values (C). A systematic relationship between dip and percent shortening (D) exists for sinusoidal folds. Calculations for the graph are based on subdividing the fold into 500 straight line segments. Modified from Jamison (1991).
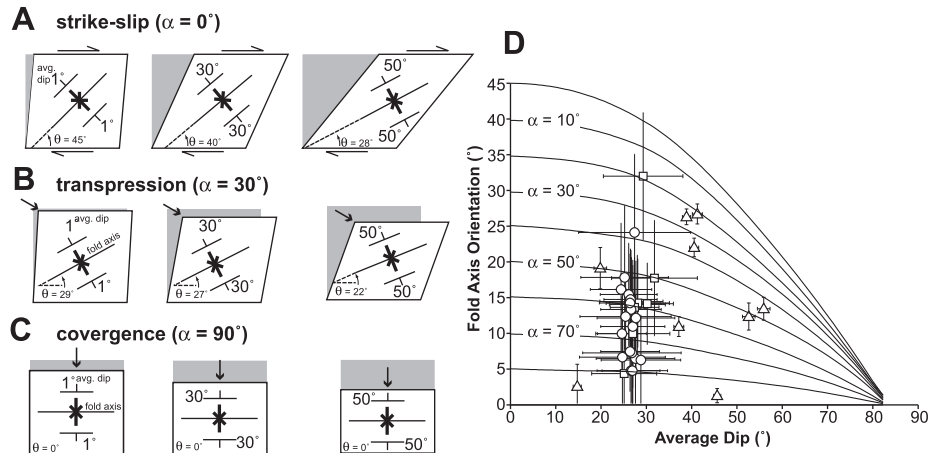
Fig. 4. Relationship between fold axis orientation and the average bedding dip of folded strata for pure strike-slip, transpressional, and purely convergent kinematics (A–C). Model results and uncertainties (D). Circles = south of the Central Range Fault; Squares = north of the Central Range Fault; Triangles = results based on bedding measurements compiled from Kugler (1960). Modified from Jamison (1991) and Titus et al. (2007).

3.6. Assessment of uncertainty

The accuracy of the strain and kinematic information produced by this approach depends directly on the accuracy of the map data used. We use a parametric bootstrap approach to propagate the uncertainties arising from the map data into our tectonic results.

3.6.1. Horizontal uncertainty

The ArcGIS geologic map used to collect the data from folded strata in the Central Range (de Verteuil et al., 2006) was digitized from the original, detailed, and unpublished 1:50,000 scale sheets of Kugler (1960). There are several potential sources of uncertainty with respect to contact location. First, if contacts were drawn on maps with a 0.5 mm pencil at a 1:50,000 scale, the contact trace lines are 25 m wide on the ground. Therefore, a point selected in the middle of the contact line is within ±12.5 m of the intended position for the contact. A second, more difficult to quantify source of uncertainty is the number and location of field observations used to constrain the position of a contact. In areas with tight geologic control, the position of a contact may in fact be somewhere within the width of the line drawn on the geologic map. The Kugler (1960) map of Trinidad was cleverly constructed using an extensive, high-density micropaleontological augering and biostratigraphy approach to deal with the poor exposure. In an effort to include the geologic uncertainty that results from such an approach, we arbitrarily assign an additional ±25 m of uncertainty (for a total of ±38 m) to the horizontal position of each contact.

3.6.2. Vertical uncertainty

The DEM used for this analysis (de Verteuil et al., 2006) was digitized from 25 m contour interval, 1:25,000 scale topographic maps. Uncertainties in the DEM arise from the digitization process itself and from errors in the original topographic maps. On a map with a 25 m contour interval, the uncertainty in elevation of a digitized point that fell in between two contour lines is ±12.5 m. This is likely an overestimate of the error involved because (1) digitization points are often selected to fall on contour lines and (2) the digitizer is unlikely to be off by a full contour interval. Nevertheless, we assume a potential uncertainty of ±13 m due to digitization in an effort to encompass the potential errors in the original topographic map data set.

3.6.3. Strike-and-dip uncertainty

Strike-and-dip measurement uncertainties are estimated using a parametric bootstrap analysis based on an approach that is commonly used in paleomagnetic analysis (see Tauxe (2002) pgs. 140–145). Each point within a data set consists of a mean and its two standard deviation uncertainty (2σ). The mean position of a contact line has x, y, and z coordinates extracted from the ArcGIS data base. These coordinates have 2σ uncertainties assumed to be ±38 m (x,y) or ±13 m (z). The mean and 2σ values for each coordinate were next used to generate a synthetic data set of with a Gaussian normal distribution. This process was repeated for each set of three observation points along every folded contact analyzed (e.g., Fig. 2).

These synthetic datasets were then used to generate estimates of strike, dip, and fold axis orientation. A set of x, y, and z coordinates were randomly chosen from the normal distribution to represent each contact position in the first iteration. The values were used to calculate a set of strike and dip data for each individual fold, which in turn were used to calculate an average bedding dip and fold axis orientation for that fold. This process was repeated for each fold, generating a population of estimates of average bedding dip and fold axis orientation. Each pair of average bedding dip and fold axis orientation was used to calculate an angle of oblique convergence and a percent fold shortening. An overall mean and 2σ uncertainty for bedding dip, angle of oblique convergence, and percent fold shortening were then calculated using standard Gaussian statistics. A mean fold axis orientation was calculated using standard Fisher statistics (e.g. Butler (1992) pg. 106–108).

Our modeling used 5000 points in a population because it produced a stable solution for each input data set. Analysis based on 500 points resulted in variation in the tenths place for the final mean bedding dip and mean fold axis orientation. Increasing the population to 5000 increased computation time only slightly and stabilizes the solution in the tenths place.

4. Model results from the Central Range Fault zone, Trinidad

4.1. Angle of oblique convergence

Transpressional kinematics in the Central Range vary from strike-slip dominated transpression (i.e. α < 20°) to almost pure contraction (i.e. α > 80°; Fig. 5; Table 1). Within uncertainty, most folds have similar average bedding dip values, so that variation in angle of oblique convergence is mostly due to variation in fold axis orientation (Fig. 4). Most folds record a strong contractional component (i.e. α > 50°), with a small group of folds located closer
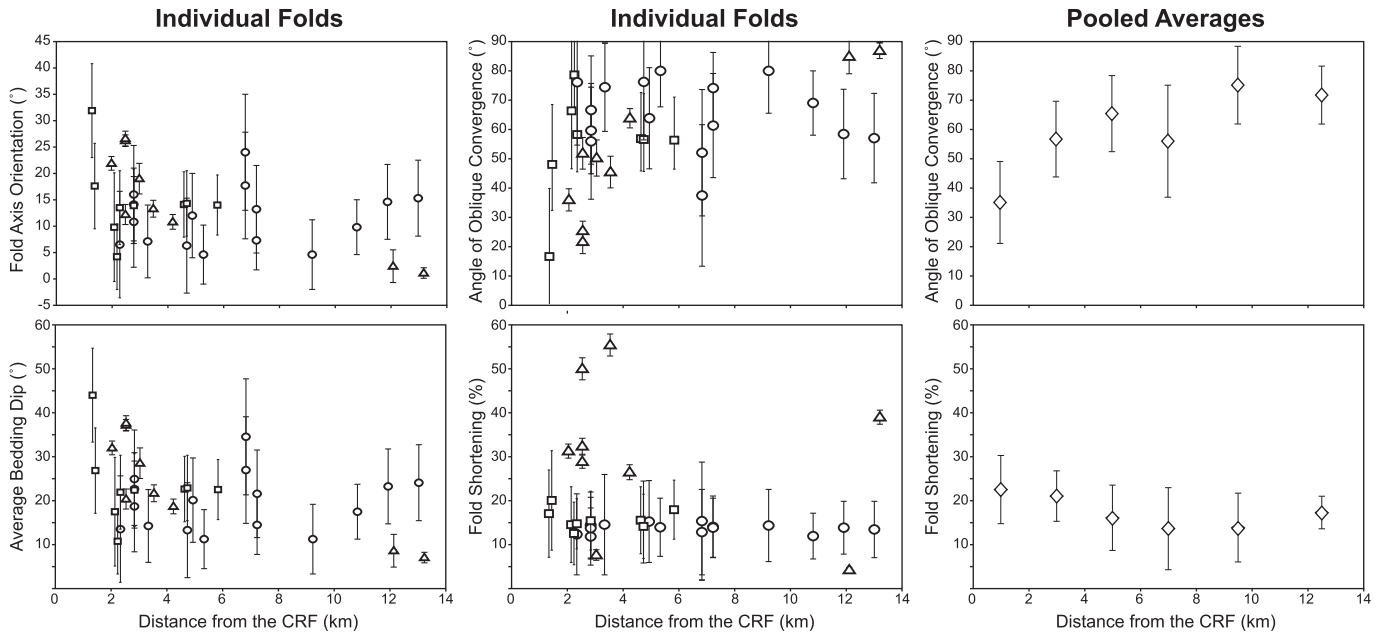
Fig. 5. Variation of fold axis, average bedding dip, angle of oblique convergence, and strain with distance from the Central Range Fault. Values are averaged in 2 km-wide zones. Circles = south of the Central Range Fault; Squares = north of the Central Range Fault; Triangles = results based on bedding measurements compiled from Kugler (1960).

Table 1
Folds in the Central Range Fault zone.

Fold number	UTM zone 20		Distance (km)	Fold axis (°)		Bedding dip (°)		α (°)		Shortening (%)	
	(mE)	(mN)		Mean	±2σ	Mean	±2σ	Mean	±2σ	Mean	±2σ
F-1	668047.9	1131763.2	13.2	1.1	1.0	45.5	0.8	86.6	2.7	38.9	1.6
F-2	672449.6	1142737.2	3.5	13.3	1.6	55.8	1.4	45.1	5.4	55.3	2.5
F-3	679021.9	1144968.2	4.2	10.8	1.4	37.0	1.1	63.5	3.3	26.4	1.7
F-4	675283.5	1149128.7	2.0	21.9	1.3	40.4	1.0	35.6	3.8	31.2	1.6
F-5	677454.2	1151239.1	3.0	19.0	2.9	19.6	1.4	49.9	6.2	7.6	1.2
F-6	684689.8	1148525.7	2.5	12.2	1.9	52.5	1.4	51.5	5.4	49.9	2.5
F-7	682097.1	1152203.8	2.5	26.2	1.1	38.7	0.9	25.0	3.3	28.8	1.5
F-8	682097.1	1152203.8	2.5	26.6	1.4	41.1	1.1	21.3	4.1	32.3	1.8
F-9	685895.8	1162635.2	12.1	2.4	3.1	14.5	0.9	84.6	5.9	4.2	0.6
S-1	689328.8	1146744.9	2.8	16.0	9.3	24.2	6.8	55.6	19.8	11.8	6.5
S-2	671762.7	1136458.7	6.8	17.7	10.1	25.0	9.7	51.7	21.6	12.8	9.7
S-3	674749.6	1137048.2	7.2	13.2	8.3	26.4	6.7	61.0	17.8	14.0	7.0
S-4	703289.6	1149876.5	4.7	6.3	9.0	27.4	8.7	75.9	19.8	15.1	9.3
S-5	705128.9	1141952.3	13.0	15.3	7.2	25.9	6.3	56.7	15.3	13.4	6.4
S-8	692754.5	1147492.5	3.3	7.1	6.9	26.6	10.9	74.1	15.1	14.5	11.4
S-9	696449.1	1147049.8	4.7	12.2	5.2	25.2	10.1	63.3	11.2	13.0	10.0
S-11	675771.5	1137827.9	6.8	24.0	11.0	27.2	12.4	37.1	24.2	15.3	13.4
S-13	701440.9	1150909.6	2.8	10.8	8.6	26.8	7.1	66.3	18.5	14.4	7.5
S-14	696975.2	1149137.5	2.8	14.1	6.9	26.2	6.8	59.3	14.8	13.7	7.0
S-15	691929.4	1142881.4	7.2	7.3	5.6	26.2	6.5	73.8	12.2	13.8	6.7
S-16	684115.1	1142437.3	5.3	4.6	5.6	26.4	6.4	79.7	12.3	13.9	6.6
S-17	673418.5	1141924.2	2.3	6.5	10.1	24.5	9.5	75.8	21.5	12.3	9.2
S-18	679483.2	1140807.2	4.9	12.0	8.0	27.5	8.6	63.5	17.3	15.2	9.3
S-20	696059.5	1140660.3	10.8	9.8	5.2	24.4	5.4	68.7	11.0	11.9	5.2
S-21	686997.2	1139318.4	9.2	4.6	6.6	26.7	7.8	79.7	14.5	14.3	8.2
N-1	693562.3	1153313.6	2.2	4.2	6.2	24.9	7.2	80.7	13.4	12.5	7.1
N-4	698745.5	1155800.5	2.8	13.9	6.9	27.8	6.2	59.3	14.8	15.4	6.7
N-7	694286.5	1157438.4	5.8	14.0	5.7	30.0	5.8	58.4	12.3	17.9	6.7
N-8	693805.1	1153191.6	2.1	9.8	10.3	26.8	8.2	68.4	22.2	14.5	8.6
N-9	698327.5	1153998.1	1.3	31.9	8.9	29.1	8.8	18.6	20.9	17.0	9.9
N-10	693824.2	1155961.5	4.6	14.1	6.2	27.9	7.0	58.9	13.4	15.5	7.6
N-16	693667.3	1155990.3	4.7	14.3	6.2	26.5	7.0	58.6	13.3	14.1	7.3
N-18	684409.3	1149618.8	1.4	17.6	8.1	31.6	9.5	50.1	18.1	20.0	11.3
N-19	699034.3	1155376.0	2.3	13.5	7.0	27.2	5.4	60.3	15.1	14.7	5.7

Note: distance = fault normal distance to the Central Range fault; fold axis = angle between the Central Range fault and the trend of the fold axis; α = angle of oblique convergence in transpression; % shortening = strain recorded by that fold, not the strain recorded by the fault zone as a whole.

Table 2
Mean vorticity and strain estimates.

Distance (km)	α (°)		Fold Sh. (%)	
	Mean	$\pm 2\sigma$	Mean	$\pm 2\sigma$
0–2	35	14	23	8
2–4	57	13	21	6
4–6	65	13	16	7
6–8	56	19	14	9
8–11	75	13	14	8
11–14	72	10	18	4

Note: distance = width of the bin measured in fault normal distance to the Central Range fault; α = mean angle of oblique convergence; fold sh. = mean % shortening of folds.

to the Central Range Fault showing a stronger strike-slip influence ($\alpha < 50°$; Fig. 5).

To clarify trends in these data, angle of oblique convergence estimates were next subdivided into groups assigned to 2 km-wide zones. The mean angle of oblique convergence estimated for each fold was pooled to produce an average for each 2-km wide zone. The upper bound of uncertainty for each zone was determined by averaging the maximum angle of oblique convergence for each individual fold in that zone. The lower bound of uncertainty for a zone was determined in the same manner (Fig. 5; Table 2). Overall, this analysis suggests that there is a narrow region within the borderlands adjacent to the master fault that has a slightly stronger strike-slip influence. Further away from the master fault, the kinematics of deformation are more contraction dominated.

4.2. Strain analysis

Shortening values for individual folds are similar throughout the borderlands (Fig. 5; Table 1). This similarity is even more pronounced when the data are pooled into the same 2 km-wide zones used above (Fig. 5; Table 2).

Next, paleo-plate motions were calculated using mean shortening and mean oblique convergence angle values from each 2 km-wide zone. The shortening recorded by individual folds was first converted to shortening across the zone following Tikoff and Peterson (1998). Shortening perpendicular to a fold axis is offset by elongation parallel to the hinge. In the case of pure wrenching ($\alpha = 0°$), the rate of contraction perpendicular to the fold hinge is balanced by the rate of elongation parallel to the fold hinge, resulting in no bulk shortening across the zone as a whole. The shortening determined for an individual fold is a reflection of the total shortening in a zone only for the special case of pure contraction ($\alpha = 90°$). For transpressional kinematics ($0 < \alpha < 90°$), the ratio of the rate of extension to the rate of contraction (ϵ_e/ϵ_c) given in Fig. 8 of Tikoff and Peterson (1998) provides a factor that can be used to scale shortening at the individual fold scale up to that of the scale of the entire shear zone. The relationship between

fold shortening (SH$_f$) and the overall shortening of the zone (SH$_z$) is given by

$$SH_z = SH_f \cdot \left(1 - \frac{\epsilon_e}{\epsilon_c}\right). \tag{3}$$

Each 2-km wide zone, represents a final length after deformation (L_f). Since both L_f and SH_z are known, the original length (L_o) was calculated by rearranging the standard percent shortening equation (eq. (4)) to solve for original lengths (eq. (5)):

$$-SH_z = \left(\frac{L_f - L_o}{L_o}\right) \cdot 100\% \tag{4}$$

$$L_0 = L_f/(1 - SH_z/100\%). \tag{5}$$

Shortening is by definition a negative elongation, therefore percent shortening was entered as negative. The amount of contractional movement (M_c) across that 2 km-wide zone is given by

$$M_c = L_o - L_f. \tag{6}$$

The amount of strike-slip movement (M_{ss}) and combined total plate motion (M_{pm}) are given by

$$M_{ss} = M_c/\tan(\alpha) \tag{7}$$

$$M_{pm} = M_c/\sin(\alpha) \tag{8}$$

where α is the angle of oblique convergence in that 2 km-wide zone.

An estimate of the maximum amount of strain recorded by the folds in the borderlands was obtained by using the maximum angle of oblique convergence and the maximum shortening for that zone. Conversely, the minimum estimate comes from using the minimum angle of oblique convergence and minimum shortening value. By combining data from folds located the same distances north and south of the master fault into the same 2-km bin we assumed that the zone is symmetrical, therefore the total amount of strain must be doubled to reflect strain across the entire zone. Overall, our strain analysis showed that folding in the borderlands records approximately 3–9 km of contraction, 3 km of strike-slip motion, and 4–9 km of total plate motion (Table 3).

5. Discussion

5.1. Model calibration and sensitivity

Detailed geologic strip maps with bedding orientation data – i.e. strike and dip measurements taken in the field – were available for six locations in the Central Range (Kugler, 1960); we also analyzed each of these six locations using the digital map data (de Verteuil
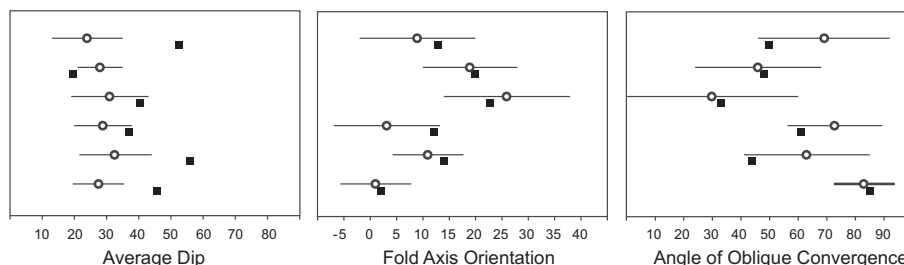

Fig. 6. GIS-based (circles) vs. field-based (squares) model results.
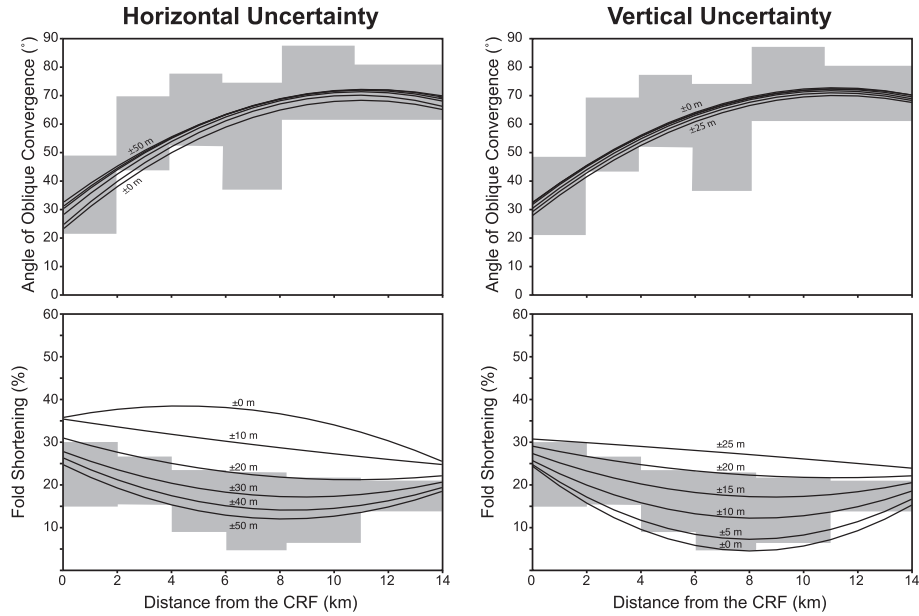
Fig. 7. Sensitivity analysis of the effect of contact uncertainty on model results. Lines show the variation of angle of oblique convergence or fold shortening across the fault zone assuming the noted uncertainty. Horizontal uncertainty plots assume a vertical uncertainty of ±13 m. Vertical uncertainty plots assume a horizontal uncertainty of ±38 m. The gray shaded region delineates the range of the pooled averages for each 2-km wide zone from Fig. 5.

et al., 2006). GIS-generated average bedding dip consistently underestimate the average bedding dips determined from the field data, while fold axis orientation and angle of oblique convergence via the two approaches yielded nearly identical results (Figs. 5 and 6). The field-based results indicated higher amounts of shortening

(i.e. steeper bedding dips) than GIS results at the same distance. In contrast, field- and GIS-based angle of oblique convergence values are similar (Fig. 5). The angle of oblique convergence determined was largely insensitive to uncertainty in contact position while the
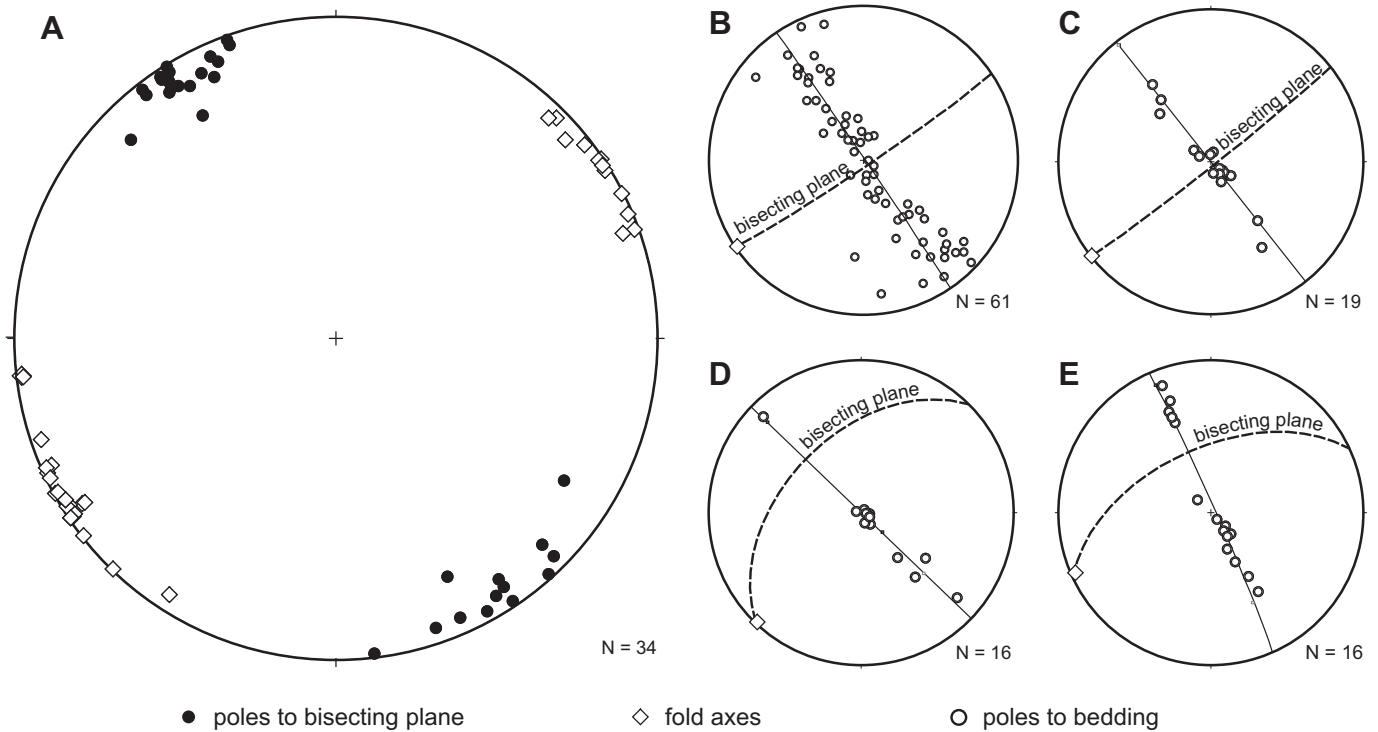
Fig. 8. (A) Summary stereonet plot of bisecting planes and fold axes for folds used in the kinematic analysis. Poles to bedding for folds N-1 (B) and S-2 (C) are representative examples showing the upper number and lower number of bedding estimates, respectively. See Fig. 1 and Table 1 for fold locations. Folds S-12 (D) and S-7 (E) are representative examples of those discarded from the analysis. The distribution of poles to bedding suggests the folds are asymmetric and moderately inclined. All plots created using Richard Allmendinger's Stereonet v.6.3.2.

Table 3
Summary of strain calculations.

Distance (km)	α (°)	Fold Sh. (%)	ϵ_e/ϵ_c	Zone Sh. (%)	Contraction (km)	Strike-slip (km)	Combined (km)
Maximum strain due to folding							
0–2	49	30	0.14	26	0.71	0.61	0.94
2–4	69	27	0.04	26	0.70	0.26	0.74
4–6	78	24	0.01	23	0.61	0.13	0.63
6–8	75	23	0.02	23	0.59	0.16	0.61
8–11	88	22	0.00	22	0.84	0.03	0.84
11–14	81	21	0.00	21	0.81	0.12	0.82
				Total × 2 =	8.5	2.6	9.2
Minimum strain due to folding							
0–2	21	15	0.49	7.7	0.17	0.43	0.46
2–4	44	16	0.19	13	0.29	0.30	0.42
4–6	52	9.1	0.12	8.0	0.17	0.13	0.22
8–10	37	4.7	0.25	3.5	0.07	0.10	0.12
8–11	62	6.5	0.06	6.1	0.19	0.10	0.22
11–14	62	14	0.06	13	0.45	0.24	0.51
				Total × 2 =	2.7	2.6	3.9

Note: distance = width of the bin measured in fault normal distance to the Central Range fault; α = angle of oblique convergence; fold sh. = % shortening recorded by folds; ϵ_e/ϵ_c = ratio of the rate of extension to the rate of contraction (from Tikoff and Peterson, 1998); Zone Sh. = % shortening for that portion of the borderlands; Contraction, Strike-slip, and Combined = km. of fault normal contraction, fault parallel strike-slip, and total movement for that portion of the borderlands; Total × 2 = sum total amount of movement doubled reflected the assumption that strain is distriubted symmetrically within the fault zone.

amount of shortening (i.e. average bedding dip) was highly dependent on this value (Fig. 7).

The GIS-based approach tends to underestimate bedding dip and shortening because much the folded contact has an apparent straight line outcrop pattern (Fig. 2). A straight contact suggests a near vertical dip, however that may not be the case if there is a low amount of relief. Any uncertainty in contact position in such a case increases the horizontal distance between adjacent points (Fig. 2), which lowers the bedding dip and estimated shortening. This is not the case in a higher relief, well-dissected structure such as the Sheep Mountain Anticline (e.g., Banerjee and Mitra, 2004). Dramatic "V's" in the contacts increase the horizontal distance between points along the contact resulting in bedding dip estimates with lower uncertainties.

An increase in the vertical uncertainty leads to higher estimated dips and shortening values (Fig. 7). In a low relief setting the change in elevation along a contact trace is nearly zero. In such a case, introduction of elevation uncertainty can only increase the change in elevation between adjacent points. If the change in horizontal position remains fixed, then an increase in the change in elevation results in the calculation of a steeper bedding dip.

Angle of oblique convergence estimates, in contrast, agree well in our field- vs. GIS-based comparison (Fig. 6), and are mostly insensitive to the uncertainty of the contact position (Fig. 7). This is primarily because the trend of any fold axis is much better constrained than the average bedding dip (Table 1). For example, visual inspection of the

geologic map clearly shows the orientation of the fold axis (Fig. 2). Because the angle of oblique convergence estimate is highly dependent on fold axis orientation at low strain (Fig. 4) there is good agreement between the field-based and GIS-based results.

The GIS results vs. field data comparison (Fig. 6) and sensitivity analysis (Fig. 7) illustrate three key points. First, average bedding dip and shortening estimates derived from a digital map data have high uncertainties in low relief terrains. The GIS-derived shortening values presented here for the Central Range have high uncertainties and are likely underestimates based on our comparisons with the same results derived from field data. Secondly, low to moderately strained folds yield fairly well constrained angle of oblique convergence estimates, despite the high degree of uncertainty in the amount of shortening. Lastly, high relief, intensely dissected structures yield more precise results. Such structures, however, are likely to be well exposed and therefore potentially accessible to the collection of traditional field measurements. In such a case, the methodology presented here would be most appropriate for use with remote sensing data and/or reconnaissance work prior to field work or in areas inaccessible for other (e.g. cost, political) reasons.

5.2. Fold shape

The results presented here assumed that the folds studied are sinusoidal, upright, shallowly plunging, and symmetric. These assumptions are necessary to use the average bedding dip of a fold
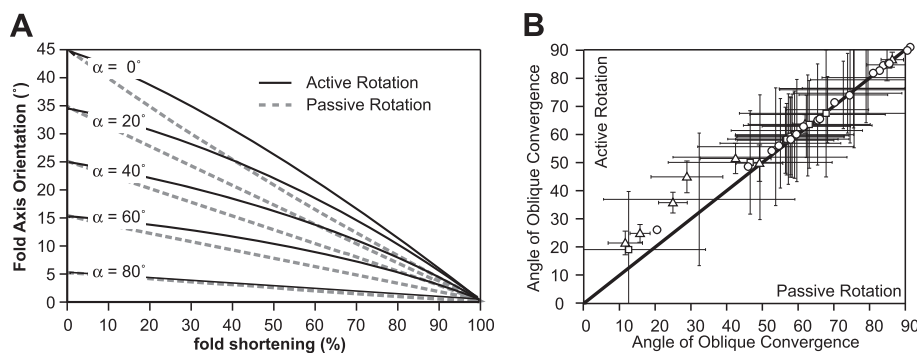
Fig. 9. Active vs. passive rotation. (A) Passive fold axes rotate into parallelism with the master fault more quickly than fold axes assumed to be active markers (from Titus et al., 2007). (B) Model results with uncertainties for active and passive rotation. The bold line marks where passive and active rotation yield the same results. Circles = south of the Central Range Fault; Squares = north of the Central Range Fault; Triangles = results based on bedding measurements compiled from Kugler (1960).

as a proxy for percent shortening (Fig. 3), but these assumptions can be evaluated using field observations, map patterns, and stereonet analysis. Folds observed in quarry exposures of the Tamana Formation (Miocene), a well-lithified limestone, are in good agreement with these assumptions. Folds observed there are upright, sinusoidal, symmetric, and shallowly plunging. All of the folds in Table 1 are characterized by map patterns similar to that displayed in Fig. 2: doubly plunging folds. Folds truncated by faults were excluded from our analysis. The map pattern displayed in Stereographic analysis of the orientation data from this fold, and all other folds analyzed in the Central Range, indicate that fold axes are nearly horizontal (i.e. <5° plunge; Fig. 8). Similarly, bisecting planes are all nearly vertical (i.e. >85° dip; Fig. 8) with poles distributed along great circle girdles, consistent with upright, symmetrical folds. Furthermore, Kugler (1960) rendered similar macrofold styles in the serial cross sections that accompany his map.

5.3. Folding vs. faulting

The range of strain values presented in Table 3 are most likely minimum estimates for the finite strain recorded in the Central Range Fault zone because these estimates were based solely on measurements taken from folded strata. Shortening recorded by faults could not be studied using the method presented here. As long as thrust faults remain blind, overlying folds will contain a record of that shortening. This is clearly not the case, however, for the Central Range (Kugler, 1960; de Verteuil et al., 2006). This suggests that our fold-based analysis provides a minimum estimate of finite strain.

5.4. Passive vs. active rotation

Fold axes can rotate either as material lines (passive markers) or rotate with the axes of the finite strain ellipsoid (active markers). Initially, material lines rotate toward a shear zone boundary faster than the axes of the finite strain ellipsoid. This means that, for a given amount of shortening recorded by a fold, a fold axis rotating as a passive marker will be closer to parallel to the shear zone boundary than a fold that has experienced the same amount of shortening but rotates as an active marker (Fig. 9). In our analysis we assume that fold hinges rotate as active markers. This leads to higher modeled estimates of the angle of oblique convergence than if passive rotation were assumed. However, the difference between these two models is small and well within the errors arising from uncertainty in contact position (Fig. 9).

5.5. Implications for Trinidad

Like many plate boundaries, the Central Range Fault zone has been the locus of multiple deformation events. Geodesy and paleoseismology indicate that the Central Range Fault zone is currently a narrow zone (15 km on either side of the fault) where elastic strain is currently being stored (Prentice et al., 2010; Weber et al., 2011). Regional analyses indicate that central Trinidad experienced a contractional (fold-and-thrust style) strain event in the Middle Miocene (e.g., Babb and Mann, 2000). Both folds and faults with geometries similar to those that we studied in central Trinidad are present in the younger Plio-Pleistocene paleo-Orinoco deltaic fill of the Southern Basin (Fig. 1). These structures are consistent with continued oblique convergence between the Caribbean-South American plates and southward propagation of the tip of the fold-thrust belt at a few millimeters per year. It is uncertain precisely when the fold-and-thrust belt style kinematics were supplanted by the modern, active transpressional kinematics of the Central Range Fault zone. The kinematic and strain analysis method applied here
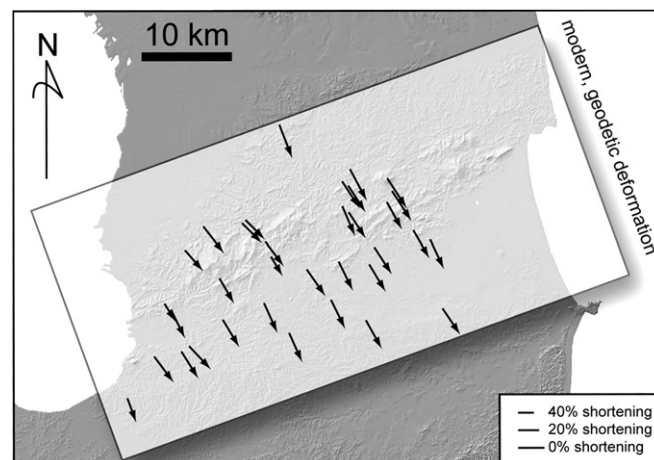
Fig. 10. Summary of strain and kinematic results. Each arrow is oriented parallel to the plate motion vector (i.e. the convergent flow apophasis) described by that particular fold. The length of the arrow is proportional to the amount of deformation recorded by that fold. Longer arrows indicate more shortening. Note that the length-shortening scale is logarithmic. All results fall within the ±15 km wide zone of modern deformation centered on the Central Range Fault as shown by elastic dislocation modeling of the geodetic data (see Weber et al., 2011). Shaded relief map from de Verteuil et al. (2006).

yielded finite strain results, making it difficult to separate active vs. ancient strain. However, our study provides the first quantitative and robust (i.e. based on results from many individual folds) estimates of paleo-plate motion estimates derived from structures within the Central Range (Fig. 10). Earlier qualitative estimates based on regional geological considerations (Pindell et al., 1998) agree well with our new estimate.

Deciphering the relationship between the long-term strain recorded in the folds of the borderlands and the short-term geodetic strain is difficult. Compilation of our results onto a fault-normal profile suggests a hint of a kinematic and/or finite strain gradient centered on the modern Central Range Fault (Fig. 5). The contractional component of deformation is greater farther away from the master fault and the intensity of the strain also increases closer to the master fault (Fig. 10). Interestingly, these trends follow the pattern of strain partitioning suggested for other, more well-studied transpressional systems such as the San Andreas Fault (Teyssier and Tikoff, 1998). However, the strain gradient across the Central Range Fault zone is within the uncertainties, which could in principle be over estimated, of our modeled results, and the cross-zone variation in angle of oblique convergence is based heavily on the results from two folds close to the Central Range Fault, which also calls into question the significance of this gradient. Within the modeled uncertainties of the results presented here the folds we analyzed in fact suggest a remarkably homogeneous strain field (Fig. 10). This implies that the modern zone of deformation has not accumulated enough permanent (non-elastic) borderland strain to overprint the pre-existing strain field. This is consistent with the idea that the Central Range Fault zone is a very young geologic feature.

6. Conclusions

Extraction of kinematic data from fold orientation and geometry using digital geologic maps and elevation datasets is a potentially powerful tool in structural geology. The GIS-based approach presented here allows for both strain and kinematic information to be gleaned relatively rapidly from a large number of folds. Analysis of large fold populations also provides the opportunity to examine

strain gradients across wide regions. This method should be applicable in any transpressional setting where high quality digital geologic maps and elevation datasets exist. Additionally, this method may prove useful in arid regions where contacts are well exposed on satellite images. A major strength lies in its remote sensing approach to structural geology. This technique could provide important first-order approximations in regions that can be refined later using more precise field-based data.

The quality of the geologic and topographic datasets used present the major limitations to this sort of "remote sensing" strain analysis technique. It is inherently difficult to quantify the uncertainty in digital geologic maps due to the original scale of the mapping, the number and distribution of primary field observations, etc. Uncertainties in elevation datasets are in general easier to quantify because of the numerical nature of this data set.

A second limitation lies in the finite strain nature of the results obtained. Like most strain analysis techniques, this method provides information only about the cumulative orientation and magnitude of strain and needs to be interpreted accordingly.

Despite significant limitations, application to the Central Range Fault zone provided a first-order picture of the finite strain field. Folds throughout the fault zone suggest a strongly convergence component to deformation ($\alpha = \sim 70°$), consistent with having formed during "fossil" oblique Caribbean-South American plate convergence. Overall, folding in the zone records a minimum of 3–9 km contraction, 3 km of strike-slip motion, and 4–9 km of total plate motion. We conclude that most of this deformation is due to earlier, Middle Miocene, fold-and-thrust style tectonic activity, rather than being the result of active strike-slip tectonism.

Acknowledgments

References

Babb, S., Mann, P., 2000. Structural and sedimentary development of a Neogene transpressional plate boundary between the Caribbean and South American plates in Trinidad and the Gulf of Paria. In: Mann, P. (Ed.), Caribbean Basins. Elsevier, Amsterdam, pp. 495–557.

Banerjee, S., Mitra, S., 2004. Remote surface mapping using orthophotos and geologic maps draped over digital elevation models: application to the sheep mountain anticline, Wyoming. American Association of Petroleum Geologists Bulletin 88, 1227–1237.

Butler, R.F., 1992. Paleomagnetism: Magnetic Domains to Geologic Terrane. Blackwell Scientific Publications, Boston.

Charlesworth, H.A.K., Langenberg, C.W., Ramsden, J., 1976. Determining axes, axial planes, and section of macroscopic folds using computer-based methods. Canadian Journal of Earth Science 13, 54–65.

de Verteuil, L., Ramlal, B., Weber, J., 2006. Trinidad Geological GIS, Module 1- Surface Geology and Geography. Latinum, Ltd., Port-of-Spain, Trinidad.

Erlich, R.N., Farfan, P.F., Hallock, P., 1993. Depositional environments, and diagenesis of the Tamana Formation, Trinidad; a tectonic marker horizon. Sedimentology 40 (4), 743–768.

Graham, R.H., 1978. Wrench faults, arcuate fold patterns and deformation in the southern French Alps. Proceedings of the Geologists' Association 89 (Part 2), 125–142.

Jamison, W.R., 1991. Kinematics of compressional fold development in convergent wrench terranes. Tectonophysics 190, 209–232.

Kugler, H., 1960. Geological Map of Trinidad with Cross-Sections Orell Fussli Arts Graphiques S.A., Switzerland, scale 1:100,000.

Lister, G.S., Williams, P.F., 1983. The partitioning of deformation in flowing rock masses. Tectonophysics 92, 1–33.

Odonne, F., Vialon, P., 1983. Analogue models of folds above a wrench fault. Tectonophysics 99, 31–46.

Perez, O.J., Bilham, R., Bendick, R., Velandia, J.R., Hernández, N., Moncayo, C., Hoyer, M., Kozuch, M., 2001. Velocity field across the southern Caribbean plate boundary and estimates of Caribbean/South American plate motion using GPS geodesy 1994-2000. Geophysical Research Letters 28, 2987–2990.

Pindell, J., Higgs, R., Dewey, J., 1998. Cenozoic palinspastic reconstruction, paleogeo- graphic evolution, and hydrocarbon setting of the northern margin of South America. In: Pindell, J., Drake, C. (Eds.), Paleogeographic Evolution and Non-glacial Eustasy, Northern South America, vol.58. SEPM Special Publication, pp. 44–85.

Prentice, C., Weber, J., Crosby, C., Ragona, D., 2010. Prehistoric earthquakes on the Caribbean-South American plate boundary, Central Range Fault, Trinidad. Geology 38 (8), 657–678. doi:10.1130/G30927.1.

Ragan, D.M., 2009. Structural Geology: An Introduction to Geometrical Techniques. Cambridge University Press.

Saleh, J., Edwards, K., Barbaste, J., Balkaransingh, S., Grant, D., Weber, J., Leong, T., 2004. On some improvements in the geodetic framework of Trinidad and Tobago. Survey Review 37, 604–625.

Sanderson, D.J., Marchini, W.R.D., 1984. Transpression. Journal of Structural Geology 6, 449–458.

Sanguinito, S., Giorgis, S., Weber, J., 2010. Constraints on the Timing of Deformation in the Central Range Fault Zone, Trinidad, from Topography and Apatite Fission Track Data [abstr.]. Geological Society of America, Annual Meeting, Paper pp.250–254.

Soto, M.D., Mann, P., Escanola, A., Wood, A.J., 2007. Late Holocene strike-slip offset of a subsurface channel interpreted from three-dimensional seismic data, eastern offshore Trinidad. Geology 35, 859–862.

Speed, R.C., 1985. Cenozoic collision of the Lesser Antilles arc and continental South America and the origin of the El Pilar fault. Tectonics 4, 41–69.

Tauxe, L., 2002. Paleomagnetic Principles and Practice. Kluwer Academic Publishers.

Teyssier, C., Tikoff, B., 1998. Strike-slip partitioned transpression of the San Andreas fault system: a lithospheric-scale approach. In: Holdsworth, R.E., Strachan, R.A., Dewey, J.F. (Eds.), Continental Transpressional and Transtensional Tectonics, vol.135. Geological Society of London Special Publication, pp. 143–158.

Teyssier, C., Tikoff, B., Markley, M., 1995. Oblique plate motion and continental tectonics. Geology 23, 447–450.

Tikoff, B., Peterson, K., 1998. Physical experiments of transpressional folding. Journal of Structural Geology 20, 661–672.

Titus, S.J., Housen, B., Tikoff, B., 2007. A kinematic model for the Rinconada fault system in central California based on structural analysis of en echelon folds and plaeomagnetism. Journal of Structural Geology 29, 961–982.

Treagus, J.E., Treagus, S.H., 1981. Folds and the strain ellipsoid: a general model. Journal of Structural Geology 3, 1–17.

Weber, J., Ferrill, D., Roden-Tice, M., 2001a. Calcite and quartz microstructural geothermometry, Northern Range, Trinidad. Journal of Structural Geology 23, 93–112.

Weber, J.C., Dixon, T.H., DeMets, C., Ambeh, W.B., Jansma, P., Mattioli, G., Saleh, J., Sella, G., Bilham, R., Perez, O., 2001b. GPS estimate of relative motion between the Caribbean and South American plates, and geological implications for Trinidad and Venezuela. Geology 29, 75–78.

Weber, J., Saleh, J., Balkaransingh, S., Dixon, T., Ambeh, W., Leong, T., Rodriguez, A., Miller, K., 2011. Triangulation-to-GPS and GPS-to-GPS geodesy in Trinidad, West Indies: neotectonics, seismic risk, and geologic implications. Journal Petroleum and Marine Geology 28, 200–211. doi:10.1016/j.marpetgeo.2009.07.010.

Zoback, M.D., Zoback, M.L., Mount, V.A., Suppe, J., Eaton, J.P., Healy, J.H., Oppenheimer, D., Reasenberg, P., Jones, L., Raleigh, C.B., Wong, I.G., Scotti, O., Wentworth, C., 1987. New evidence on the state of stress of the San Andreas Fault System. Science 238, 1105–1111.